energies

MDPI

Article

Microscopic Pore-Throat Mobilization Characteristics and Conversion Timing Strategies for CO_2 Injection After Waterflooding in Reservoirs with Different Properties: A Case Study of Block X, Huabei Oilfield

Hongmei Wang [1], Hong Chen [2], Hongtao Wang [1], Yu Sun [3,4], Yiqiang Li [3,4,*], Yafan Xing [1] and Zhaoyang Lu [1]

1 Exploration and Development Research Institute, PetroChina Huabei Oilfield Company, Renqiu 062552, China
2 PetroChina Huabei Oilfield Company, Renqiu 062552, China
3 State Key Laboratory of Petroleum Resources and Engineering, China University of Petroleum, Beijing 102249, China
4 College of Petroleum Engineering, China University of Petroleum, Beijing 102249, China
* Correspondence: yiqiangli@cup.edu.cn

Abstract

Due to varying development histories of reservoirs with different physical properties in Block X, Huabei Oilfield, the remaining oil distribution and microscopic mobilization limits after waterflooding remain unclear, and the subsequent CO_2 transition timing urgently requires clarification. In this study, high-temperature and high-pressure core displacement experiments combined with online nuclear magnetic resonance (NMR) were conducted to simulate CO_2 injection after waterflooding to water cuts of 50%, 80%, and 100% and compared with continuous gas injection (CGI) to reveal the effect of different switching timings on the oil recovery and pore-throat mobilization for the three reservoir classes tested in this study. Results indicate that waterflooding primarily mobilizes pores larger than 0.1 μm, while crude oil in small pores (<0.1 μm) is difficult to effectively displace. After switching to CO_2 flooding, the mobilization efficiency across all pore-throat classes increases significantly, with Class IV reservoirs exhibiting the largest enhancement in micropore recovery—from 5.8% after waterflooding to 34.5% after CO_2 flooding, representing an increment of approximately 28.70 percentage points—demonstrating that CO_2 can significantly expand the effective mobilization range relative to waterflooding. The underlying microscopic mechanism is that the degree of waterflooding alters the oil–water distribution within the core: at low-water-cut stages, remaining oil is continuously distributed, allowing injected CO_2 to contact crude oil through sufficient diffusion and dissolution, which is interpreted as providing a mobility-control effect that helps suppress gas channeling; at high-water-cut stages, remaining oil is segmented and trapped in micropores, limiting CO_2–crude oil contact, while long-term waterflooding establishes preferential water pathways that promote localized gas channeling and restrict mass transfer. These findings provide experimental evidence for the class-specific design of post-waterflooding CO_2 injection strategies.

Keywords: CO_2 flooding; post-waterflooding transition timing; NMR; microscopic pore-throat mobilization; injection strategy design

Academic Editor: Nikolaos Koukouzas

Received: 11 August 2026
Revised: 16 September 2026
Accepted: 17 September 2026
Published: 18 September 2026

1. Introduction

As a conventional secondary oil recovery technique, waterflooding generally faces the challenges of high water cuts and low economic efficiency in the late stage of development. A large amount of remaining oil exists in immobilized microscopic pore-throat structures in the form of clusters or films [1], which is difficult to effectively mobilize by conventional waterflooding methods [2–4]. With the advancement of the national dual-carbon goals (carbon peak and carbon neutrality), carbon capture, utilization, and storage (CCUS), or CO_2-enhanced oil recovery and geological storage integration technology, has become a key technical pathway for efficiency enhancement, cost reduction, and green transformation in oilfields [5] due to its dual advantages of enhanced oil recovery (EOR) and carbon emission reduction. Transitioning to CO_2 miscible flooding in the late stage of waterflooding development can not only improve the macro-displacement efficiency by reducing the oil–water interfacial tension and supplementing formation energy but also significantly enhance the microscopic displacement efficiency through the extraction and viscosity reduction of light components in crude oil by supercritical CO_2 [6–11], thereby achieving the deep potential tapping of remaining oil after waterflooding. Clarifying the essential differences in oil recovery between waterflooding and CO_2 flooding serves as the basis for demonstrating the necessity of transitioning to CO_2 flooding after waterflooding. Scholars at home and abroad have conducted systematic studies on this issue from two scales: macro-displacement efficiency and microscopic pore-throat mobilization through physical simulations. Guo et al. [12] used a long-core physical model to conduct comparative displacement experiments on three modes: complete waterflooding, continuous CO_2 miscible flooding after complete waterflooding, and initial continuous CO_2 miscible flooding. The results showed that the ultimate oil recovery of complete waterflooding was 42.15%, that of complete CO_2 miscible flooding was 69.21%, and that of continuous CO_2 miscible flooding after complete waterflooding was 75.0%, indicating that transitioning to CO_2 flooding after waterflooding can further improve oil recovery. Xiao et al. [13] found by comparing the NMR signals of different injection media that both waterflooding and gas flooding mainly mobilize oil in large pores, whereas the transition from waterflooding to gas flooding can effectively mobilize a portion of crude oil in small pores due to the broader sweep efficiency of CO_2. Zhou et al. [14] compared the displacement behaviors of waterflooding and CO_2 flooding in heterogeneous channels using molecular dynamic methods and found that CO_2 flooding had the lowest threshold pressure gradient; during waterflooding, injected water preferentially flowed along large-sized channels, making it difficult to effectively mobilize the crude oil in small-sized channels. The above studies confirm from both the macro-recovery and microscopic pore-throat mobilization perspectives that CO_2 flooding is superior to waterflooding in terms of recovery efficiency, and transitioning to CO_2 flooding after waterflooding still holds significant potential for oil increment, providing the necessary experimental basis for implementing CO_2 flooding after waterflooding.

However, how to determine the appropriate timing for transitioning to CO_2 flooding among the tested conditions and define the minimum pore-throat boundary that can be effectively driven by CO_2 are core issues in formulating scientific CO_2 injection strategies [15,16]. Premature transition may lead to an unstable CO_2 displacement front and premature gas channeling, resulting in a low displacement efficiency and poor economic performance [17]. Conversely, a delayed transition may cause formation energy exhaustion and the excessive dispersion of remaining oil, hindering mass transfer between CO_2 and crude oil, making it difficult to achieve effective miscibility and thereby restricting the full play of the EOR potential of CO_2 [18–20]. Li et al. [15] found through systematic core displacement experiments that the optimal transition timing for tertiary CO_2 flooding is when waterflooding reaches half of its maximum secondary oil recovery, at which point the subsequent CO_2 breakthrough time is significantly delayed and the recovery based on residual oil is substantially improved. Based on numerical simulation research of typical high-water-cut reservoirs in Shengli Oilfield, Liu et al. [20] pointed out, from the perspective of net present value (NPV), that when the gas price is 0.178/m^3 and the carbon subsidy is 0.0169/m^3, the optimal timing for transitioning from waterflooding to CO_2 injection should be earlier than a water cut of 82%. Meanwhile, the microscopic pore structure and fluid distribution of reservoirs after waterflooding are extremely complex, and injected gas is prone to severe gas channeling along high-permeability channels or water-channeling pathways, resulting in low sweep efficiency [21,22]. The authors of [23] systematically investigated the channeling effects of different injection modes in heterogeneous reservoirs using parallel long-core displacement experiments combined with NMR technology and found that significant differences in reservoir properties make conventional waterflooding extremely prone to inducing channeling, with injected fluids preferentially flowing along high-permeability zones while bypassing oil-bearing low-permeability regions. Yan et al. [24] studied the controlling mechanism of heterogeneity on gas-channeling pathways using two-dimensional visual physical models; the experiments showed that CO_2 preferentially migrates horizontally along high-permeability layers and laterally channels into low-permeability layers through non-intercalation interfaces after breakthrough, whereas injection from the non-intercalation side induces vertical gas channeling. In addition, although the presence of the water phase can alleviate gas channeling, its negative effect lies in the fact that the water phase may prevent part of the crude oil from being contacted by CO_2, thereby reducing the displacement efficiency. In low-permeability reservoirs, it is difficult for gas to break through the water-lock barrier in microscopic pores, resulting in high driving resistance and limited displacement efficiency [25–27]. Cui [28] studied the microscopic interaction process between CO_2 and remaining oil under high-water-cut conditions using a high-temperature and high-pressure microscopic visualization experimental setup. The results showed that the shielding effect of water significantly delayed the microscopic contact process between CO_2 and crude oil, complicating the miscibility process. However, regardless of the water film thickness, CO_2 can penetrate the water film and dissolve in the remaining oil; the higher the injection pressure, the faster the diffusion rate of CO_2 and the shorter the time required to achieve miscibility. Lu et al. [29] revealed the microscopic mechanism of CO_2 displacing residual oil in water-bearing dead-end nanopores through molecular dynamic simulation, finding that oil-phase displacement can only be initiated after the water film is broken. The hydrogen-bonding interaction between water molecules and the rock surface, as well as the dissolution of CO_2 molecules in water, are key factors in disrupting the hydrogen bond network between water molecules and facilitating water film breakthrough.

Traditional macro-core displacement can only obtain macroscopic indicators such as the gas–oil ratio, pressure dynamics, and ultimate recovery, making it difficult to reveal the seepage mechanism and mobilization limits of CO_2 in micro/nanopores and throats. The introduction of low-field NMR scanning technology provides a powerful in situ monitoring method for quantitatively evaluating the dynamic evolution of hydrogen nuclear signals in pores and throats of different pore sizes, enabling the fine characterization of the remaining oil distribution after waterflooding and fluid migration and the mobilization characteristics during CO_2 displacement at the pore scale [30,31]. Wang et al. [32] used NMR to study the microscopic remaining oil distribution in ultra-low-permeability reservoirs, and the results showed that the remaining oil in hydrophilic reservoirs is distributed in medium-to-large pores, while in oleophilic reservoirs, it is distributed in medium-to-small pores. Javad Siavashi et al. [33] utilized NMR technology to study fluid displacement and distribution during waterflooding in carbonate cores, providing flow patterns of internal pore structures throughout the oil displacement process, thereby achieving a better and comprehensive understanding of EOR simulation. Xiao et al. [34] investigated the crude oil recovery in pores of different sizes within ultra-low-permeability cores under different gas injection schemes through core displacement and NMR relaxation measurements, and they quantified the oil recovery and residual oil distribution in pores of different sizes. Zhao et al. [35] performed experimental core displacement evaluations of waterflooding and CO_2 flooding using NMR technology, revealing the dynamic distribution information of oil, water, and sc-CO_2 during the core displacement process. Zhao et al. [36] integrated online NMR displacement and high-pressure mercury intrusion (HPMI) experiments to systematically compare the pore-throat mobilization rates of high-, medium-, and low-permeability cores at different displacement stages. They found that during the waterflooding stage, high- and medium-permeability cores mainly mobilized micropores (mobilization rates of 60.02–80.11%), whereas during the CO_2 miscible flooding stage, the full pore-throat mobilization rates of medium- and low-permeability cores (17.09–31.49%) were significantly higher than those of high-permeability cores (14.57–16.63%), and the EOR of CO_2 flooding showed a strong negative correlation with the permeability, average pore-throat radius, and sorting coefficient ($R^2 \geq 0.80$). Su [37] further established a novel conversion method based on NMR T_2 spectra and high-pressure mercury intrusion data, clarifying that supercritical CO_2 miscible flooding can effectively mobilize pore throats smaller than 3.7 nm (with a mobilization rate of up to 73%), whereas non-miscible flooding only achieves a mobilization rate of about 35% for pore throats smaller than 10 nm. Qi et al. [38] realized the visualization and quantitative monitoring of internal fluid distribution and migration patterns in sandstone during CO_2 flooding using online low-field NMR technology, revealing the dominant role of the pore structure in influencing the CO_2 displacement efficiency and clarifying the specific mechanisms of factors such as pressure, temperature, permeability, and crude oil viscosity on the crude oil recovery contribution in pores of different scales.

To address the above issues, this study is designed to answer three questions: (1) Can CO_2 injection improve recovery after waterflooding? (2) Does the transition timing (fw = 50%, 80%, or 100%) affect this improvement? (3) Is the effect dependent on the reservoir class (II, III, or IV)? To answer these questions, this study conducted coupled experimental research on high-temperature and high-pressure core displacement and online NMR scanning, targeting the issues of unclear pore-throat mobilization boundaries and ambiguous gas injection strategies caused by varying degrees of waterflooding development among different reservoir types (Classes II, III, and IV) in Block X, Huabei Oilfield. This work provides experimental insights into the interaction between waterflooding and CO_2 flooding and offers theoretical references for field CO_2 injection strategies, which is valuable for maximizing remaining oil recovery after waterflooding. However, the conclusions of this study are primarily applicable to the evaluation of CO_2-enhanced oil recovery (EOR) performance, and the CO_2 storage potential was not quantitatively assessed in this work. The experiments took three waterflooding stages with produced fluid water cuts of 50%, 80%, and 100% as the main variables and compared them with the CGI mode. By comparatively analyzing the T_2 spectrum evolution characteristics, recovery contribution rates of pore throats at all levels, and macroscopic displacement dynamics (oil recovery, gas–oil ratio, and breakthrough front) of reservoirs with different physical properties during waterflooding and transition to CO_2 injection, this paper systematically elucidates the microscopic pore-throat mobilization lower limits and microscopic oil–water distribution mechanisms of waterflooding and CO_2 flooding, aiming to provide a theoretical basis and experimental support for the precise formulation of post-waterflooding CO_2 injection strategies and the deep potential tapping of remaining oil in similar oilfields.

2. Experimental Methods and Materials

The target block is Block X, Huabei Oilfield, with formation pressures ranging from 47.36 to 58.63 MPa and reservoir temperatures ranging from 116 to 149 °C, classifying it as a high-temperature reservoir. The reservoirs predominantly have medium-to-high permeability, with average porosities of 14.5–21.0% and average permeabilities of 39.2–146.2 mD.

2.1. Experimental Materials and Equipment

The experimental oil sample was obtained from Well 1-62X in Block X, Huabei Oilfield. Under reservoir temperature and pressure conditions, the formation oil density is 0.8408 g/cm^3 and the formation oil viscosity is 5.412 mPa·s. The minimum miscibility pressure (MMP) between CO_2 and the crude oil is 44 MPa. The MMP was determined by slim-tube tests performed by the project partner at reservoir temperature (150 °C), and the value of 44 MPa was provided by the operator. All experiments were performed at a constant temperature of 150 °C in a thermostatic oven, with an outlet backpressure of 50 MPa to target miscible CO_2 conditions. Both waterflooding and CO_2 flooding were conducted at a constant injection rate of 0.1 mL/min. A confining pressure of 52 MPa was applied throughout the tests to prevent fluid channeling along the core sidewall. The inlet and outlet pressures were recorded in real time, and the differential pressure was monitored to track flood-front advancement and identify the onset of gas channeling. During the CO_2 injection stage, the measured differential pressure remained between 0.1 and 1.0 MPa across all reservoir classes, corresponding to inlet pressures of 50.1–51.0 MPa and macroscopic pore pressures exceeding 50 MPa throughout the core. However, recognizing that bulk slim-tube MMP measurements (44 MPa) and outlet backpressure control do not definitively prove that the in situ pressure stayed above the effective miscibility threshold along the entire core length (particularly under the severe capillary resistance and potential pore-confinement shifts in Class IV reservoirs), all gas-flooding experiments in this study are described as being conducted under intended miscible conditions based on an outlet backpressure above the MMP. A 2000 ppm $MnCl_2$ solution (salinity 2000 ppm) was used as the aqueous phase for both waterflooding and core saturation prior to gas flooding, consistent with the water composition used in the online NMR tests to suppress the hydrogen signal from water. Prior to the formal experiments, we conducted blank NMR scans on cores saturated with the $MnCl_2$ solution without oil; the water signal was completely suppressed (no detectable signal in the T_2 spectrum), confirming that the 2000 ppm concentration is sufficient to effectively shield the water signal. It should also be noted that this $MnCl_2$ solution serves only as an NMR signal suppressor; its salinity and ionic composition differ from those of the actual formation water, and therefore it does not represent formation water. The 2000 ppm $MnCl_2$ solution used as the paramagnetic agent may slightly affect wettability and interfacial tension. Although the effect at this low concentration (0.2 wt%) is expected to be limited, it cannot be fully excluded. Since the same solution was used in all comparative experiments, any systematic effect is consistent across tests and therefore does not affect the relative trends or the comparisons among the tested schemes. Future work should evaluate these potential effects using representative formation water. The natural cores used in this study were all collected from Block X of the Huabei Oilfield, with a coring depth of approximately 4234–4921 m, and have a diameter of 2.5 cm with individual lengths ranging from 5 to 10 cm. The cleaning, drying, and determination of the fundamental petrophysical properties—such as the porosity and permeability—were conducted in accordance with API RP 40, Practices for core analysis, and the results are summarized in Table 1. Specifically, short cores with a length of 5 cm were used for the online displacement-coupled NMR experiments (Nos. 1–3 in Table 1); for each reservoir class, the same short core was scanned at multiple displacement stages.

No independent replicate plugs were available; therefore, the pore-throat recovery values are single-core observations. Spliced long cores of ~30 cm in length were used for the high-temperature and high-pressure long-core displacement experiments, assembled by placing four natural plugs of ~7.5–8.5 cm in length end to end (Nos. 4–15 in Table 1), with multiple layers of filter paper inserted between adjacent plugs to reduce the capillary end effect at the core interfaces. This assembly is intended to approximate the flow behavior of an intact natural long core; however, the interfaces between plugs may still introduce some uncertainty into the displacement behavior, which should be acknowledged. The specific assembly combinations for each reservoir class are indicated in the "Experiment Type" column of Table 1. It should be noted that, to minimize the interference of core heterogeneity on comparisons among different switching schemes, the same set of spliced cores was used for all long-core displacement schemes within each reservoir class. These tests are therefore not independent experimental replicates but controlled comparisons using the same core matrix. After completing each test, the natural cores were cleaned by Soxhlet extraction, dried, and re-measured for gas permeability and porosity. The variations in porosity and permeability before and after cleaning were strictly controlled within 2%, indicating that the core properties were essentially restored to their initial states, allowing the same cores to be reused for subsequent schemes. This approach maximizes the elimination of systematic deviations caused by core heterogeneity and ensures that the horizontal comparisons among different CO_2 switching timings are conducted under strictly controlled conditions. The petrophysical properties of all individual plugs used in the long-core assemblies are fully listed in Table 1, allowing readers to independently assess the representativeness of the experiments. The injection gas was CO_2 with a purity of 99%. The experimental equipment mainly included an ISCO high-precision syringe pump (Teledyne ISCO, Lincoln, NE, USA), a multi-functional long-core displacement system (Yangzhou Huabao Petroleum Technology Co., Jiangsu, China.), an online low-field NMR scanning system (Spake Technology Development Co., Beijing, China.), as well as high-pressure pistons, pressure sensors, backpressure regulators, constant-temperature ovens, gas flow meters, data acquisition systems, valves, pipelines, and six-way valves, as shown in Figure 1. The spatial resolution of the low-field NMR imaging system used in this study is approximately 0.5 mm × 0.5 mm, which is sufficient to distinguish oil–water distribution changes at the core scale (core diameter: 25 mm) but cannot resolve fluid distribution at the single-pore scale. In the core holder, fluorinated oil was used as the confining pressure transmission medium; because it contains no hydrogen nuclei (^1H), it produces no NMR signal and therefore does not interfere with the detection of oil and water signals during online NMR measurements.

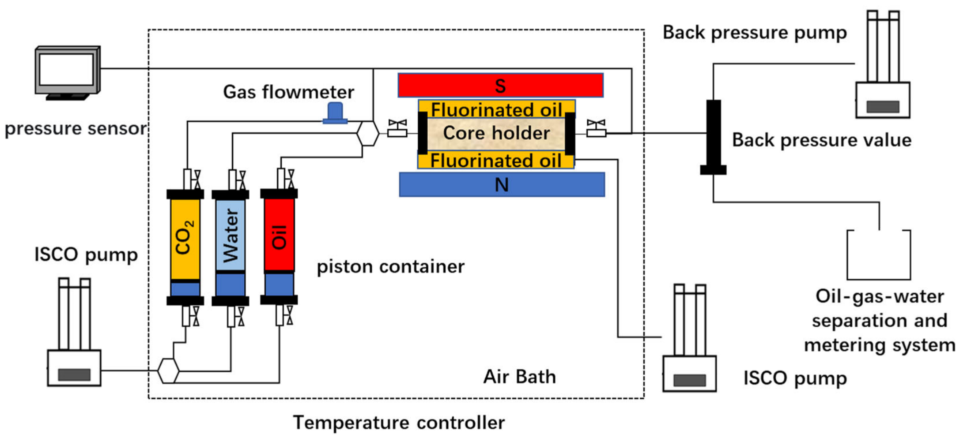

Figure 1. Diagram of experimental apparatus.

Table 1. Basic parameters of experimental cores.

No.	Length (cm)	Permeability (mD)	Porosity (%)	Field Reservoir Classification Result	Experiment Type
1	5.04	10.81	14.45	IV	NMR (IV short core, same core scanned at multiple stages)
2	5.02	78.68	18.92	III	NMR (III short core, same core scanned at multiple stages)
3	5.0	170.35	20.34	II	NMR (II short core, same core scanned at multiple stages)
4	7.99	11.54	13.9	IV	Long-core assembly (IV)
5	6.96	10.31	14.37	IV	Long-core assembly (IV)
6	7.00	10.07	13.92	IV	Long-core assembly (IV)
7	8.53	14.25	14.85	IV	Long-core assembly (IV)
8	7.92	83.17	19.17	III	Long-core assembly (III)
9	8.11	82.54	18.72	III	Long-core assembly (III)
10	8.00	80.5	18.95	III	Long-core assembly (III)
11	7.65	86.23	19.05	III	Long-core assembly (III)
12	7.99	156.9	19.98	II	Long-core assembly (II)
13	8.86	163.1	20.32	II	Long-core assembly (II)
14	7.86	164.8	20.44	II	Long-core assembly (II)
15	8.35	168.6	20.52	II	Long-core assembly (II)

2.2. Experimental Methods and Procedures

First, online displacement-coupled NMR experiments were conducted using 5 cm short cores. Based on the classical surface relaxation mechanism, $1/T_2 = C/r$, the conversion coefficient (C) was determined by interpolating and fitting the cumulative NMR T_2 spectrum curve in the initial saturated state with the high-pressure mercury intrusion capillary pressure curve using the least-squares method. Given the inherent differences in pore structures and rock surface relaxivities among various reservoir types, independent calibrations were performed for each category—C = 42.6 μm/s for Class II reservoir cores, C = 43.1 μm/s for Class III reservoirs, and C = 43.8 μm/s for Class IV reservoirs—thereby ensuring the reliability of the classification into micropores, mesopores, and macropores, as summarized in Table 2. According to the pore-throat radius distribution, the pore throats were classified into small pores (0.01 μm–0.1 μm), medium pores (0.1 μm–1 μm), and large pores (1 μm–10 μm). It should be noted that the classification thresholds of 0.1 μm and 1 μm follow the generally accepted pore-throat classification standards in petroleum geology. This classification primarily serves as a relative comparison among different reservoir classes, highlighting the order-of-magnitude differences in the pore radii rather than representing absolute physical boundaries. A sensitivity check using adjusted thresholds (0.05/0.5 μm and 0.2/2 μm) confirmed that the relative trends among reservoir classes remain unchanged, and the main conclusions are not significantly affected by the specific choices. The detailed results of this sensitivity analysis are provided in Supplementary Table S1, which serves strictly as a trend robustness check rather than as proof of direct nano-scale observation, given that the calibration-dependent T_2 conversion does not resolve individual pores. NMR scans were performed on the three types of reservoirs at five stages: completion of oil saturation, waterflooding to produced fluid water cuts of 50%, 80%, and 100%, and completion of gas flooding. NMR imaging was utilized to observe the oil–water distribution at different stages. It should be noted that these two types of experiments serve distinct purposes in this study. The NMR experiments on short cores are designed to reveal the evolution of pore-throat oil saturation during waterflooding (at F_w = 50%, 80%, and 100%) and the ultimate mobilization capacity of CO_2 after waterflooding. They are not intended to evaluate the performance of different transition timings because the cores switched at 50% and 80% water cuts were not scanned after CO_2 injection. The long-core displacement experiments, in contrast, provide the primary basis for evaluating the recovery performance of different transition timings, and the recovery performance and cumulative gas–oil ratio (CGOR) dynamics at different water-cut switching points will be presented in Section 3.2. The CGOR is defined as the ratio of cumulative gas produced to cumulative oil produced (volume measured under standard conditions, 20 °C, 1 atm). First, gas breakthrough is identified as the moment when CO_2 gas is first detected at the outlet, corresponding to the point where the CGOR curve begins to deviate from zero. It should be noted that the CGOR trajectory and recovery curve shape serve as indirect macroscopic indicators of breakthrough; a subsequent rapid rise in the CGOR indicates that the production response is consistent with intensified preferential gas flow and early gas breakthrough and is not a direct measurement of internal channeling paths. Subsequently, spliced long cores were used to analyze the transition timing. To ensure comparability, the gas injection volume in the CO_2 flooding stage (conducted under the intended miscible conditions) was maintained at 2HCPV (Hydrocarbon Pore Volume) for all tests.

Table 2. Summary of T_2-to-equivalent throat radius conversion calibration parameters for NMR tests.

No.	C	Conversion Relationship	R^2
1	42.6	$r = T_2/42.6$	0.9238
2	43.1	$r = T_2/43.1$	0.9168
3	43.8	$r = T_2/43.8$	0.9091

The experimental procedures for the online displacement-coupled NMR experiments include: (1) Equipment parameter debugging: Place the sample into the equipment, perform frequency calibration on the NMR system, adjust the pulse amplitude, and set parameters such as the echo time, waiting time, and number of scans. (2) Natural core cleaning and drying: Measure the core dimensions and determine the gas permeability. Vacuum-treat the core for more than 12 h and then saturate it with an $MnCl_2$ aqueous solution at a concentration of 2000 ppm to shield the NMR signal of water and calculate the porosity. (3) Core oil saturation: Saturate the core with oil at a rate of 0.05 mL/min. After oil appears at the production end, increase the injection rate to achieve a better saturation effect. Set the experimental backpressure to 50 MPa (simulating the initial formation pressure) and continue oil injection to raise the internal pressure of the core to the required experimental pressure until the backpressure regulator discharges fluid normally. Calculate the oil saturation and perform an NMR T_2 spectrum scan to obtain the initial oil-saturated state of the core. (4) Waterflooding stage: Set the required injection rate and initiate the waterflooding experiment. Record experimental data such as the time, pressure, and production. Stop injection after the water cut of the effluent at the outlet end meets the experimental requirements. Specifically, when the produced water cut reaches 100%, continue water injection until no oil is detected for an additional 1 PV (with an oil detection limit of <0.1 mL), which is taken as the endpoint of waterflooding. Then, initiate the NMR T_2 spectrum scan. (5) Gas flooding stage: Set the injection parameters according to the experimental scheme, start the displacement experiment, and record the experimental parameters. Continue the displacement until only gas and no oil is produced and then initiate the NMR T_2 spectrum scan and conclude the experiment. The experimental procedures for the high-temperature and high-pressure long-core post-waterflooding CO_2 transition experiments are similar to those of the online displacement-coupled NMR experiments, except that step (1) and the subsequent NMR T_2 spectrum scans are omitted. It should be noted that the water-cut values (F_w = 50%, 80%, and 100%) refer to the water fractions in the produced fluid at which waterflooding was terminated; these values should not be confused with the in situ water saturation (Sw) within the core.

3. Results and Discussion

3.1. Analysis of Pore-Throat Mobilization Characteristics in Different Types of Reservoirs

CO_2 dissolution in crude oil can cause oil swelling and alter the T_2 relaxation behavior, which may affect the NMR signal distribution. Although all experiments were conducted under constant temperature and backpressure to keep the CO_2 solubility consistent, a dedicated calibration of crude oil before and after CO_2 saturation was not performed; this limitation should be recognized. Therefore, the cumulative T_2 signal amplitude was used only as a relative indicator of the oil content/saturation, and the NMR signal should not be interpreted as directly reflecting oil saturation or as resolving the water film thickness, fluid interface morphology, or local fluid composition, as shown in Figure 2. The curves represent different displacement stages: initial oil saturation, F_w = 50%, F_w = 80%, F_w = 100%, and after CO_2 flooding. It should be noted that the NMR observations presented in this section reflect the oil–water distribution at the end of each waterflooding stage (F_w = 50%, 80%, and 100%) rather than the post-CO_2 injection state for the 50% and 80% switching schemes.

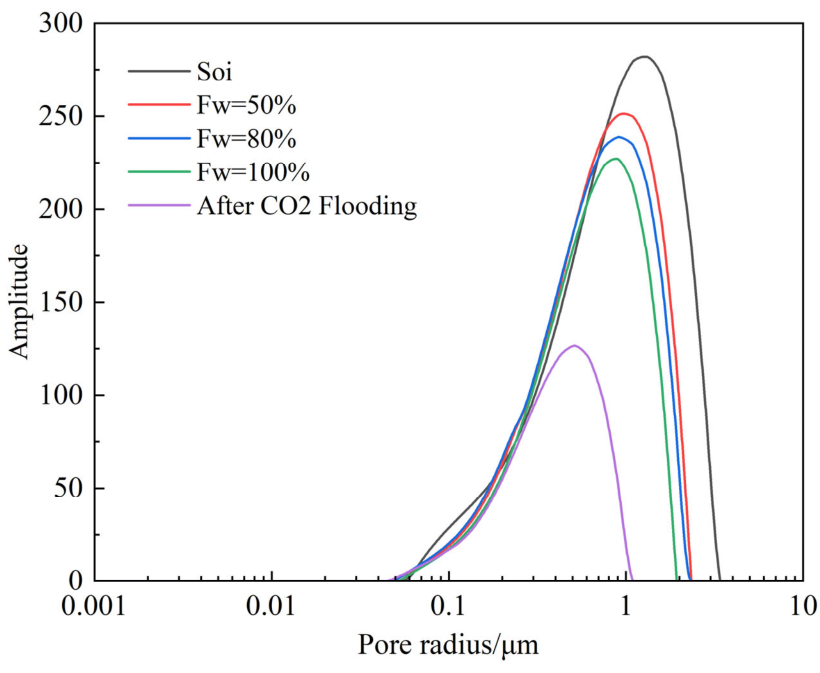

Figure 2. Nuclear magnetic resonance scanning results of Class II reservoir cores.

With the increase in the degree of waterflooding, as the produced fluid water cut rises from 50% to 100%, the NMR signal curves representing the oil saturation within pore throats exhibit regular evolution: the peaks continuously shift to the right, and the overall amplitude decreases significantly. The medium-to-large pore throats (1 μm–10 μm) in the core are progressively swept, and crude oil is displaced. By the end of waterflooding (F_w = 100%), the signal in the large pore-throat interval approaches the background value. After CO_2 flooding, the signal intensity of the curve across the entire pore-throat distribution range (0.001 μm–10 μm) drops to the global minimum. Especially in the micropore throat range of 0.01 μm–0.1 μm, the signal becomes completely flat and significantly lower than that at any waterflooding stage, demonstrating that CO_2 flooding achieves a more thorough mobilization of the entire pore system. CO_2 possesses the characteristics of low viscosity and low interfacial tension and can achieve miscibility with crude oil, significantly reducing capillary resistance. In addition, the strong diffusion and dissolution capacity of CO_2 in crude oil enables it to enter micropore throats blocked by the water phase through mass transfer, thereby effectively displacing the crude oil therein and realizing more uniform microscopic displacement.

Figure 3 shows the NMR scanning results of Class III reservoir cores at different displacement stages. With the progress of waterflooding (F_w increasing from 50% to 100%), the signal peaks of the curves gradually shift to the right and shrink toward the lower-amplitude region, indicating that the crude oil in the medium-to-large pore throats (0.1 μm–10 μm) is progressively displaced. By the end of waterflooding (F_w = 100%), the signal of the curve in the larger pore-throat interval has significantly decreased. After CO_2 flooding, the overall signal amplitude of the curve drops to the lowest across the entire pore-throat range, especially in the micropore throat range of 0.01 μm–0.1 μm, where the signal is lower than that of the waterflooding curve at any stage, demonstrating that CO_2 flooding achieves a more thorough mobilization of the core pore space.

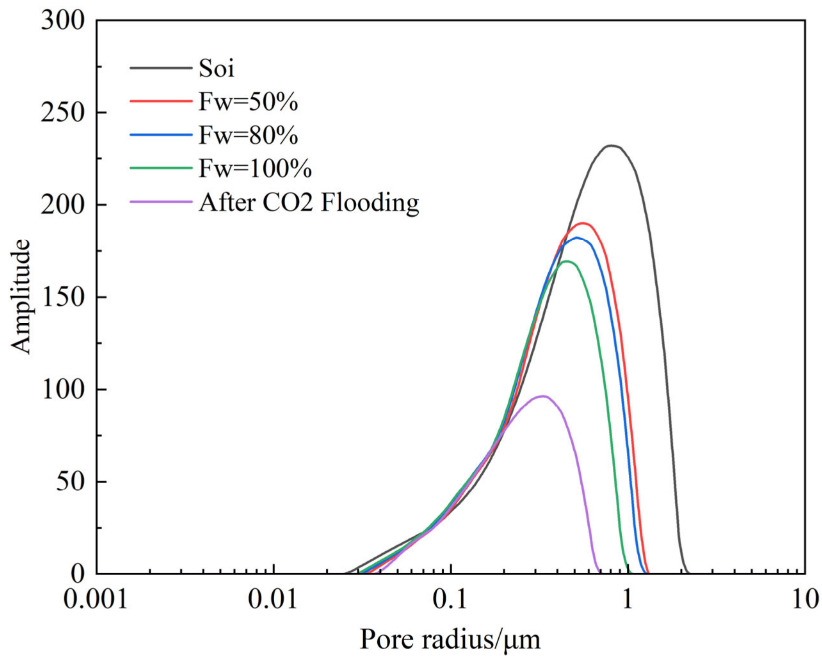

Figure 3. Nuclear magnetic resonance scanning results of Class III reservoir cores.

Figure 4 shows the NMR scanning results of Class IV reservoir cores. During the waterflooding stage, as the produced-fluid water cut (Fw) increases from 50% to 100%, the curves representing different displacement stages exhibit an overall systematic rightward shift, and the signal amplitude in the medium-to-large pore-throat interval (0.1–10 μm) decreases significantly. By F_w = 100%, the signal in the large pore-throat region has dropped to an extremely low level, indicating that the mobilization of medium-to-large pore throats by waterflooding is relatively thorough. Compared with waterflooding, the curve after CO_2 flooding shifts further to the right overall, and the signal amplitude across the entire pore-throat range (especially in the 0.01–1 μm interval) drops to even lower levels. This indicates that CO_2 flooding can not only continue to drive the remaining oil left in large pore throats after waterflooding but, more importantly, also exhibits extremely a strong mobilization capacity in micropore-throat regions. Waterflooding relies primarily on pressure differential drive and is greatly influenced by fluid viscosity and interfacial tension. Class IV reservoirs have poor physical properties, with extremely high capillary resistance in micropore throats, making it difficult for the water phase to overcome this resistance to enter. Consequently, preferential channels are prone to form along medium-to-large pore throats with lower flow resistance, leading to uneven microscopic sweep efficiency and a large amount of remaining oil trapped in small pores.

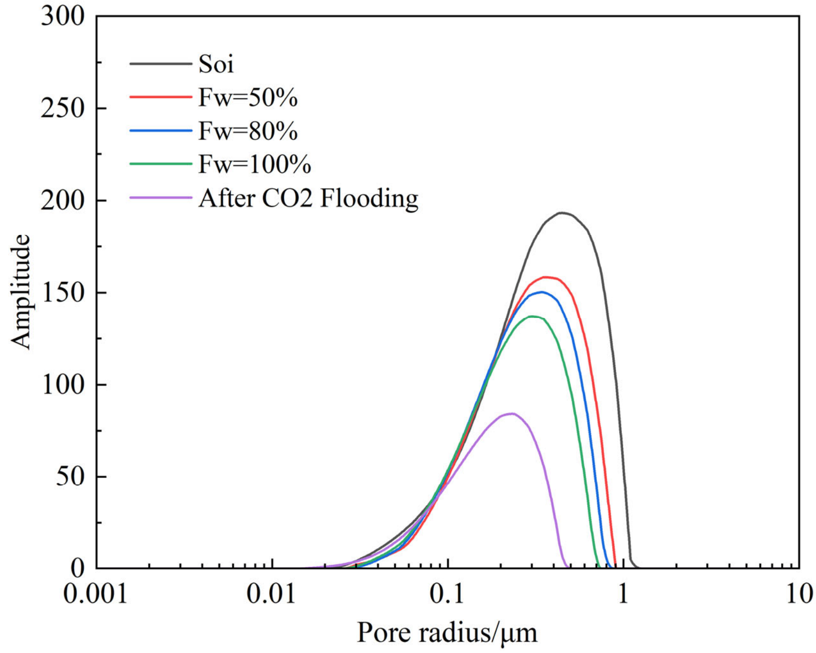

Figure 4. Nuclear magnetic resonance scanning results of Class IV reservoir cores.

To evaluate the NMR-derived oil saturation trends, the cumulative oil production observed at the outlet was compared with the oil saturation decreases inferred from the NMR signal during the short-core experiments. The two sets of data show consistent trends, especially during the CO_2 flooding stage, indicating that the reduction in the NMR signal is qualitatively consistent with oil production instead of solely reflecting oil redistribution or relaxation behavior changes caused by CO_2 dissolution. Since the $MnCl_2$ solution was used to shield the water signal, the NMR signal predominantly represents the oil phase. However, because the produced oil volume from the short cores was too small for precise volumetric metering at the outlet, this comparison serves as a qualitative consistency check rather than as a quantitative mass-balance validation.

Figure 5 shows the comparison of the pore-throat mobilization across different scales. From the perspective of microscopic pore-throat mobilization characteristics, during the waterflooding process, the recovery efficiency of large pores increases from 80% at F_w = 50% to approximately 96.84% at F_w = 100%. The recovery efficiency of medium pores increases from 19% to approximately 38%. The recovery efficiency of small pores remains at the lowest level throughout, slowly increasing from 8% to about 20%. Even at the end of waterflooding, about 80% of the initial crude oil in small pores remains unproduced, constituting the primary storage space for the waterflooding remaining oil. The waterflooding process exhibits a clear mobilization sequence of large pores → medium pores → small pores, with the mobilization degree decreasing sharply step by step. This intuitively reflects the law that flow resistance increases exponentially as the pore-throat radius decreases. After CO_2 flooding, the oil recovery efficiencies across all three T_2-derived pore-size classes achieve dramatic enhancements, and the mobilization uniformity is significantly improved. The recovery efficiency of small pores rises to 35%. The recovery efficiency of medium pores increases from about 38% to nearly 69%, showing the largest magnitude of increase. The recovery efficiency of large pores is also further optimized from approximately 96.84% to approximately 98.35%. By substantially enhancing the oil recovery efficiency of medium-to-small pore throats—especially small pores—CO_2 flooding precisely and efficiently mobilizes the remaining oil enrichment zones left by waterflooding.

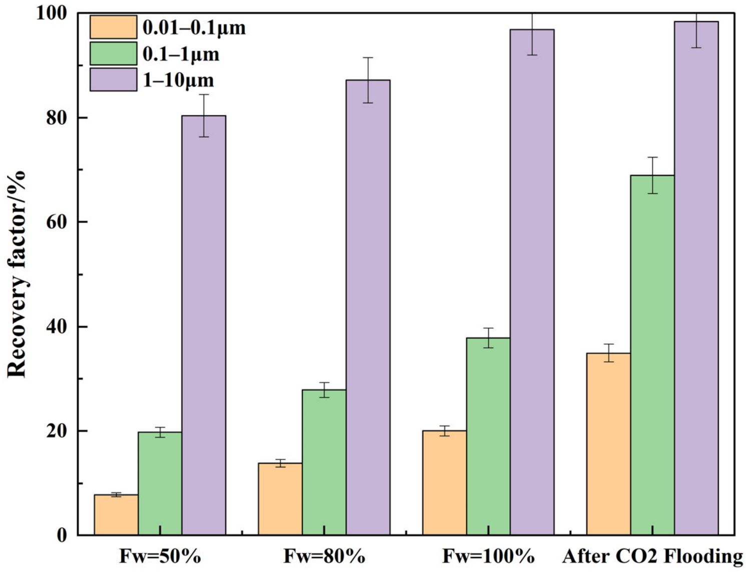

Figure 5. Bar chart of pore-throat mobilization in Class II reservoir cores.

Compared with Class II reservoirs, Class III reservoirs exhibit a slower mobilization of pore throats smaller than 1 μm, and the corresponding results are shown in Figure 6. During the waterflooding stage, the recovery efficiency of medium pores steadily increases from about 17% to around 28%, but the ultimate efficiency still shows a significant gap compared to that of large pores. The recovery efficiency of small pores remains the lowest throughout, slowly increasing from about 7% to 19%. Even at the end of waterflooding, about 80% of the initial crude oil in small pores remains unproduced, becoming the enrichment zone of the waterflooding remaining oil. Upon the completion of waterflooding, the remaining oil is highly concentrated in small pores and partial medium pores. Small pores and medium pores retain approximately 80% and 72% of the initial reserves, respectively, making them the primary potential-tapping targets for enhanced oil recovery. After CO_2 flooding, the microscopic mobilization uniformity across the three T_2-inferred pore size classes is fundamentally improved. The recovery efficiency of small pores increases to about 32%, with an increment exceeding 13 percentage points. The recovery efficiency of medium pores increases from about 28% to nearly 54%, showing the most significant enhancement.

Compared with the first two types of reservoirs, the overall mobilization degree of Class IV reservoirs is significantly lower than that of medium-to-high-permeability cores, and the corresponding results are shown in Figure 7. During the waterflooding stage in Class IV reservoirs, the recovery efficiency of small pores is extremely low, with a recovery degree of only 5.8%, and over 90% of the crude oil remains trapped within small pores. The recovery efficiency of medium pores increases gently from 5.7% to 16%. The recovery efficiency of large pores increases from 36.5% to 57%, indicating that even under low-permeability conditions, waterflooding still possesses a certain displacement capacity for large pore throats. After CO_2 flooding, the recovery efficiency of small pores increases to about 34.5%, with an increment as high as 29 percentage points, showing a significant improvement. The recovery efficiency of medium pores leaps from about 16.6% to about 34.7%. The recovery efficiency of large pores further increases from about 57% to about 98%, approaching complete production.

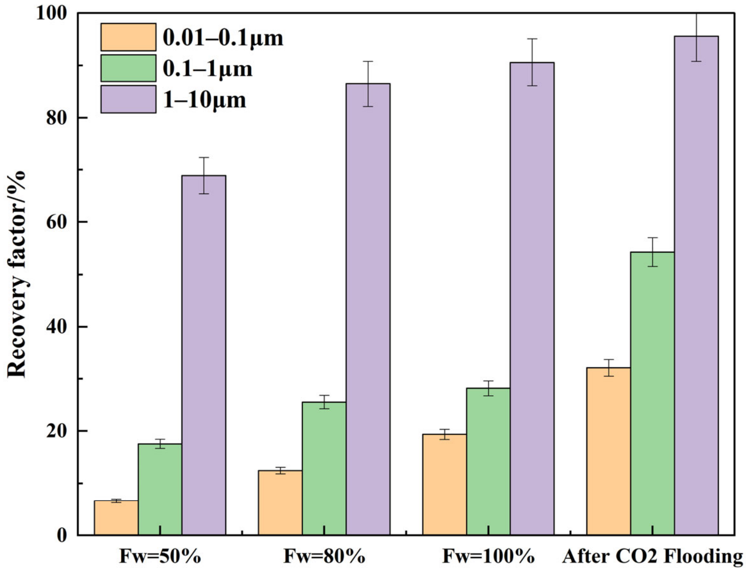

Figure 6. Bar chart of pore-throat mobilization in Class III reservoir cores.

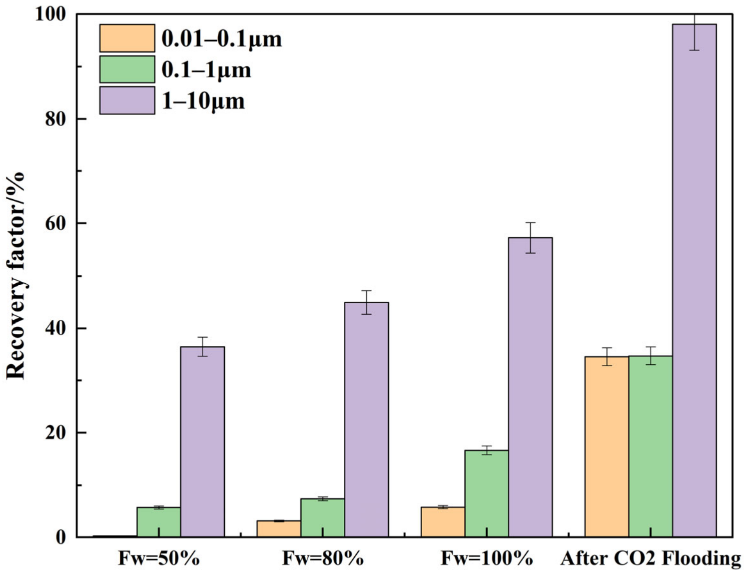

Figure 7. Bar chart of pore-throat mobilization in Class IV reservoir cores.

During the waterflooding process, the signal of large pores drops sharply with the advancement of waterflooding, indicating more thorough mobilization and less remaining oil at the end of waterflooding. The signal of medium pores decreases significantly, indicating that waterflooding has a favorable displacement effect on pore throats in this interval. At the end of waterflooding, a strong signal still exists in the small pore interval, showing that a large amount of crude oil in micropores remains immobilized, making it the primary remaining oil enrichment zone of waterflooding. Even under high-permeability conditions, the mobilization capacity of conventional waterflooding for small pores is still limited, and the problem of incomplete microscopic displacement caused by mobilization limits is widespread. CO_2 flooding can significantly compensate for the deficiencies of waterflooding, further lower the mobilization limit to effectively mobilize the crude oil retained in micropore throats after waterflooding, and achieve further utilization of the pore space. This confirms that CO_2 exhibits a superior ability to overcome capillary resistance, access smaller pore throats, and mobilize microscopic remaining oil, significantly enhancing pore-scale oil-washing efficiency. Therefore, sequential CO_2 flooding after waterflooding is a key subsequent technology for improving microscopic sweep efficiency and tapping the potential of remaining oil.

Class II cores are selected as the representative example for NMR imaging because their favorable porosity and permeability allow for the clearest visualization of flood-front advancement and water channel evolution, whereas the lower signal-to-noise ratios in Class III and IV low-permeability cores limit the spatial resolution of 2D imaging during online displacement. By identifying hydrogen signals to determine the oil saturation distribution within the core, and taking Class II reservoirs as an example, comparing the NMR scan images at different water cuts during waterflooding allows for an intuitive tracking of the advancement of the displacement front and changes in the remaining oil distribution, as shown in Figure 8. Red represents the oil phase, with darker colors indicating higher oil saturation in that region. In the initial oil-saturated state, the core presents an overall dark-red color, indicating that crude oil fills the entire pore space. With the progress of waterflooding, the red color at the injection end (lower side) first begins to lighten or non-red regions appear, showing significant differences in the oil displacement efficiency across different positions of the core. At a water cut of 50%, the water phase has formed a distinct front, with large areas of medium-to-light-red regions behind it, indicating that a considerable amount of remaining oil is still distributed in continuous or semi-continuous states. As the water injection volume increases, the area near the injection end turns light red or non-red, and the remaining oil in the middle and rear parts of the core is segmented into discontinuous dark-red patches. When the water cut reaches 80%, several preferential flow paths with virtually no red color appear, surrounded by red regions, leading to uneven sweep efficiency. By the end of the waterflooding stage, the blocky remaining oil at the inlet end is mobilized, but the remaining oil in the middle and rear parts of the core is segmented into discontinuous dark-red patches (mainly located in the middle of the core), while patchy or isolated red patches still exist near the production end, representing microscopic remaining oil bypassed or immobilized by waterflooding. Compared with waterflooding, the overall red color of the core after CO_2 flooding further lightens and its range shrinks, with the dark-red patches remaining after waterflooding is significantly reduced or completely has disappeared. This suggests that through diffusion, viscosity reduction via dissolution, and miscibility mechanisms, CO_2 can enter pore spaces inaccessible to the water phase, thereby further enhancing oil recovery.

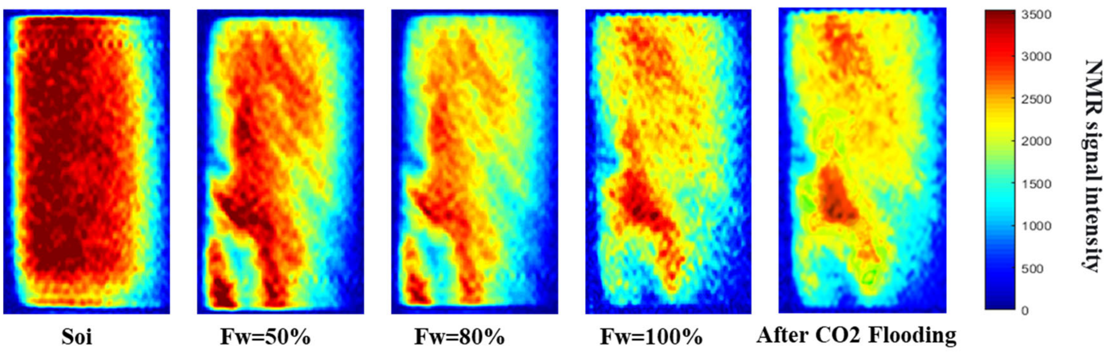

Figure 8. NMR imaging of Class II reservoir cores.

According to the fractional flow equation, as water saturation increases, the relative permeability of the water k_{rw} increases while that of the oil k_{ro} decreases, leading to the enhanced mobility of the water phase. During post-waterflooding gas injection, the flow of CO_2 is more susceptible to pressure gradient control. When waterflooding reaches a water cut of 100%, the k_{rw} approaches its maximum, and water flow becomes completely dominant, with the water phase occupying most of the pore network in a continuous distribution. Inferred from the rapid rise in the water cut and the decline in the oil production rate, the production performance indicates that a continuous water-dominated flow path has been established. At this stage, the injected CO_2 tends to advance along the path of least resistance, and subsequent gas injection is highly prone to channeling along the high-permeability channels formed by the continuously distributed water phase. The contact interface between CO_2 and crude oil is relatively limited, which hinders the full utilization of diffusion and mass transfer advantages and easily leads to gas channeling. When the water cut is 50%, the relative permeabilities of the oil and water phases are in a relatively balanced range. Water-channeling pathways have not yet formed, and the oil phase distribution remains relatively continuous. Meanwhile, the water phase in the pores is in a dispersed state. Following CO_2 injection, the mobility-control effect that is suggested by the observed displacement performance may facilitate sufficient diffusion and mass transfer with the remaining oil, thereby delaying gas channeling. Therefore, the key to formulating a post-waterflooding CO_2 injection strategy lies in selecting the appropriate transition timing based on different reservoir physical properties. This suggests that the dispersed water phase may exert a mobility-control effect, while also promoting diffusion and mass transfer between CO_2 and the dispersed remaining oil, ultimately achieving the highest oil recovery efficiency. It must be noted that inferences regarding relative permeability changes (k_{rw}/k_{ro}), continuous water pathways, and mobility control are interpretations of the macroscopic production response, rather than measured in-situ water saturation (S_w) or relative-permeability data.

3.2. Analysis of Experimental Results of High-Temperature and High-Pressure Long-Core Post-Waterflooding CO_2 Transition Flooding

By analyzing the dynamic responses of different types of reservoirs during waterflooding and gas flooding processes, it can be found that their production performance is closely related to reservoir physical properties and pore structures. Experiments on transitioning to CO_2 flooding after waterflooding to different water cuts were conducted using cores from three types of reservoirs, and the results were compared with CGI. Among the switching points investigated, the recovery performance and CGOR were analyzed through the recovery degree and CGOR, and the experimental results for Class II reservoir cores are shown in Figure 9. In the early stage of injection (<0.15 HCPV), the CGI scheme exhibits a slightly lagging slope in the increase of recovery degree due to the time required to establish oil-gas mass transfer. In contrast, the post-waterflooding CO_2 transition schemes start with a higher baseline recovery degree at the beginning of the gas flooding stage, inheriting the foundation established by the preceding waterflooding. Among them, for the F_w = 100% scheme, after transitioning from waterflooding to gas flooding, the recovery degree shows the smallest increment because most of the movable oil has already been swept away by waterflooding and long-term water flushing tends to create preferential water-flow paths, as indicated by the flattening of the recovery curve. The F_w = 50% scheme demonstrates an exceptional capacity for enhancing oil recovery, with the recovery degree rising rapidly after the transition and eventually reaching a peak of 78.11%. The reason is that when the water cut reaches 50%, oil and water coexist within the reservoir, and the remaining oil is distributed in a continuous or semi-continuous state. When CO_2 is injected at this point, destructive water-channeling pathways have not yet formed, and a moderate movable water saturation is present. The water phase is considered to provide a mobility-control effect, which may force CO_2 to sweep medium-to-small pores more uniformly; meanwhile, CO_2 can undergo efficient diffusion, dissolution, and extraction with the continuously distributed remaining oil, achieving the ultimate efficiency of water-gas synergistic sequential displacement and allowing its ultimate recovery efficiency (78.11%) to even exceed that of continuous gas injection (75.53%). As the degree of waterflooding deepens further to 80% or even 100%, long-term water flushing causes the crude oil to be severely fragmented and trapped within micropores, transforming the oil phase from continuous to extremely dispersed. Meanwhile, the water phase becomes fully interconnected within high-permeability channels, forming preferential water-flow paths. When transitioning to CO_2 injection at this stage, the rapid rise in the CGOR and the leveling of recovery are consistent with early gas breakthrough and preferential flow along these swept paths, which limits gas–oil contact, reduces mass transfer efficiency, and yields a lower final recovery of 71.19%. Due to the large pore-throat radii in high-permeability reservoirs, continuous CO_2 injection lacks the mobility control provided by the water phase, causing gas channeling to occur at an extremely early stage (approximately 0.55 HCPV). When the gas injection volume reaches 0.82 HCPV, the slope of the CGOR curve reaches its maximum, soaring to approximately 900 mL/mL, which indicates severe gas channeling and low effective gas utilization under continuous gas injection. Compared with continuous gas injection, for the post-waterflooding CO_2 transition flooding, the recovery degree increases relatively quickly during the early waterflooding stage, as higher porosity and permeability are conducive to fluid flow, allowing higher oil recovery to usually be achieved during both the waterflooding and gas-flooding stages. However, this type of reservoir also tends to face strong heterogeneity and high-permeability channels, which easily induce water channeling. Once water breaks through, the water cut increases rapidly, and the oil production rate drops sharply until the production end predominantly produces water with negligible oil production. After transitioning to CO_2, the water phase retained within the pores during waterflooding is considered to act as a mobility-control slug, increasing the flow resistance of the gas phase and suppressing the premature breakthrough of CO_2. Especially when F_w = 100%, the water phase fills most of the pore network, resulting in the most pronounced delay in gas channeling and the slowest rise in the CGOR. Here, the inferred moderate movable water saturation, continuous water pathways, and mobility-control effects are interpretations of the effluent production response and differential pressure dynamics, not the measured in situ S_w or relative-permeability data.

In the 80 mD medium-permeability reservoir, due to the decreased matrix permeability and reduced pore-throat size compared to the 170 mD reservoir, the flow resistance during direct pure CO_2 injection is relatively increased, and the occurrence of gas channeling is slightly delayed compared to the 170 mD reservoir. However, after the injection volume reaches the mid-to-late stage (approximately 0.7 HCPV), due to the lack of mobility control by the water phase, gas channeling occurs, resulting in a final recovery efficiency of 71.60%; the corresponding results are shown in Figure 10. In the post-waterflooding CO_2 transition schemes, as the produced-fluid water cut (F_w increasing from 50% to 100%) at the transition timing increases, the effect of delaying gas channeling gradually becomes more pronounced. Among the post-waterflood switching schemes, the Fw = 50% scheme achieved the highest recovery (71.70%), which is essentially comparable to that of CGI (71.60%), with the growth rate of the recovery degree after gas transition being significantly faster than those of other schemes. For the F_w = 50% transition scheme, the coexistence state of oil and water in the reservoir is ideal at this point, the remaining oil has not been excessively washed by waterflooding, and the production response is consistent with the absence of dominant preferential water pathways. The injection of CO_2 can fully play the roles of diffusion, mass transfer, extraction, and miscible displacement. Meanwhile, the moderate water saturation provides a favorable mobility-control effect, contributing to the highest ultimate

https://doi.org/10.3390/en19184432

recovery efficiency. For the F_w = 100% scheme, after undergoing the entire waterflooding process, most of the movable oil has already been produced during the waterflooding stage. After gas transition, the flattening of the recovery growth curve may be partly attributed to the high water saturation and associated water-locking effects, which inhibit the energy supply and light component extraction functions of gas flooding. However, other factors such as limited injectivity and poor phase connectivity may also contribute to this behavior. During transition at the high-water-cut stage, microscopic remaining oil is mostly trapped in medium-to-fine pore throats with high capillary resistance, and the continuous blockage formed by the water phase hinders the direct contact between the gas and crude oil, thereby impairing the gas flooding performance. These deduced internal flow mechanisms, including moderate water saturation, mobility control, and continuous water blockage, represent interpretations of production data, not measured S_w or relative-permeability effects.

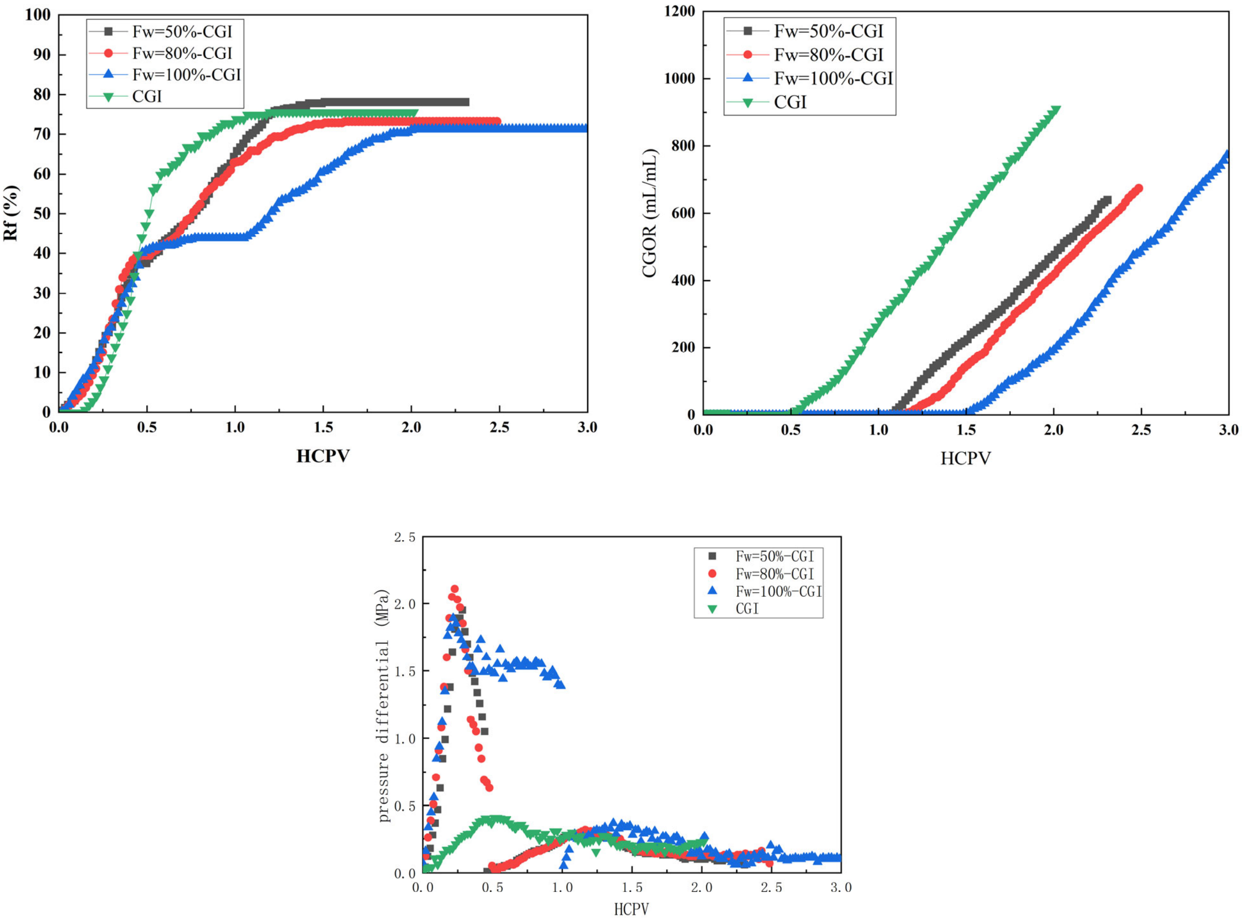

Figure 9. Core displacement experimental results of Class II reservoir cores.

For Class IV reservoirs with fine pore throats and poor physical properties, the same transition timing faces completely different challenges. Due to the small average pore-throat radius, relatively tight pore structure, and high capillary resistance in Class IV reservoirs, the gas-channeling point during direct CO_2 injection is significantly delayed compared to medium-to-high-permeability reservoirs (at approximately 0.8 HCPV). However, due to the strong heterogeneity of micropore throats in low-permeability cores, once the gas breaks through, the CGOR soars rapidly, and its value is significantly higher than that of medium-to-high-permeability reservoirs, with the final recovery efficiency of direct CO_2 injection reaching 66%; this comparative result is illustrated in Figure 11. In the post-waterflooding CO_2 transition schemes, during the waterflooding stage, a larger production pressure differential is required to drive fluid flow. When transitioning to gas injection development, a considerable amount of movable water still remains in the reservoir, and these water phases hinder the establishment of an effective displacement relationship between the gas and crude oil, causing crude oil production to fail to respond rapidly and resulting in a significant lagging phenomenon. Meanwhile, due to their inherent strong hydrophilicity and extremely high capillary resistance, it is difficult for the injected gas to effectively break through the continuous water barrier formed by movable water. The water phase forms a barrier within the micropore throats, severely impeding the physical contact between CO_2 and the trapped crude oil, which greatly weakens the key extraction, diffusion, and dissolution mechanisms. Meanwhile, water-locking effects are considered to be one of the possible contributing factors that may prevent the gas from effectively displacing and driving the crude oils. Other factors, including limited pore connectivity and capillary end effects, may further complicate the displacement process. This not only reduces the mobility of crude oil but also significantly weakens the extraction and miscible displacement effects of CO_2 on crude oil, thereby constraining the ultimate recovery efficiency of this type of reservoir. Therefore, even with the transition to gas injection, the ultimate recovery efficiency basically remains at the level of the end of waterflooding, with a recovery efficiency of 61.43%. The macroscopic results above are not contradictory to the microscopic mobilization capacity of CO_2 revealed by NMR for Class IV reservoirs. The NMR experiments (Figures 4 and 7) show that the small-pore recovery increases from 5.8% after waterflooding to 34.5% after CO_2 flooding, reflecting the ultimate microscopic displacement capacity of CO_2. However, the long-core F_w = 100% switching scheme yields negligible macroscopic incremental recovery. This apparent contradiction can be explained from three aspects. First, the absolute oil content in micropores is limited, so even a substantial relative increase in small-pore recovery contributes little to total recovery in absolute terms. Second, high capillary pressure and water-locking effects may inhibit effective CO_2–oil contact and mass transfer. Third, in the short NMR cores (5 cm), the diffusion distance is short, allowing mobilized oil to reach the outlet more easily; in the long cores (30 cm), the diffusion distance is six times longer, and the mobilized oil struggles to overcome capillary resistance to form a continuous oil phase. Meanwhile, pressure monitoring data show that the pressure differential stabilized after waterflooding and showed no significant decline after CO_2 injection, indicating that the injected gas failed to establish an effective displacement pressure gradient—further supporting the above interpretation. Therefore, the NMR results demonstrate the microscopic potential of CO_2, while the macroscopic results reflect practical constraints of transport and connectivity—the two are complementary rather than contradictory. It should be stressed that descriptions such as continuous water barriers and water locking are interpretations of the observed production lag and pressure curves rather than measured saturation or relative-permeability data.

Comparing the experimental results of the 10 mD low-permeability layer, 80 mD medium-permeability layer, and 170 mD high-permeability layer, the transition scheme at a water cut of 50% achieved the highest recovery among the tested conditions for the high-permeability layer (170 mD) and medium-permeability layer (80 mD). Class II reservoirs exhibit the most significant enhancement; with well-developed large pore throats, waterflooding can rapidly carry away movable oil, and at F_w = 50%, the water phase is considered to provide favorable mobility control with excellent water–gas synergy, yielding a recovery efficiency that even exceeds that of the CGI development scheme. This superiority stems from the fact that under this transition timing, the fluid distribution and flow state within the reservoir achieve an ideal dynamic equilibrium. At a water cut of 50%, the production response is consistent with the absence of stable, high-permeability preferential flow pathways such that gas injection does not immediately result in severe preferential gas flow or early breakthrough. Under these conditions, the movable water phase inferred to be present in the pore network may provide favorable mobility control. It partially occupies the larger pores, forcing the subsequently injected CO_2 gas to enter medium-to-small pores more extensively and contact the remaining oil therein, thereby significantly reducing the relative permeability of the gas, effectively controlling gas mobility, suppressing the premature occurrence of gas channeling, and enhancing the sweep volume and displacement efficiency of the gas. For Class II reservoirs with favorable physical properties, oil and water coexist within the pores at this stage, with a moderate movable water saturation. The injected CO_2 can not only undergo effective mass transfer and extraction with the crude oil but can also achieve a smoother displacement front with the assistance of the water phase. This water–gas synergistic microscopic displacement mechanism is far more efficient than continuous gas injection or gas transition at the high-water-cut stage. As with the earlier interpretations, this postulated water–gas synergy and mobility control by a water slug are deductions from macroscopic recovery trends, not directly measured saturation distributions or relative-permeability characteristics.

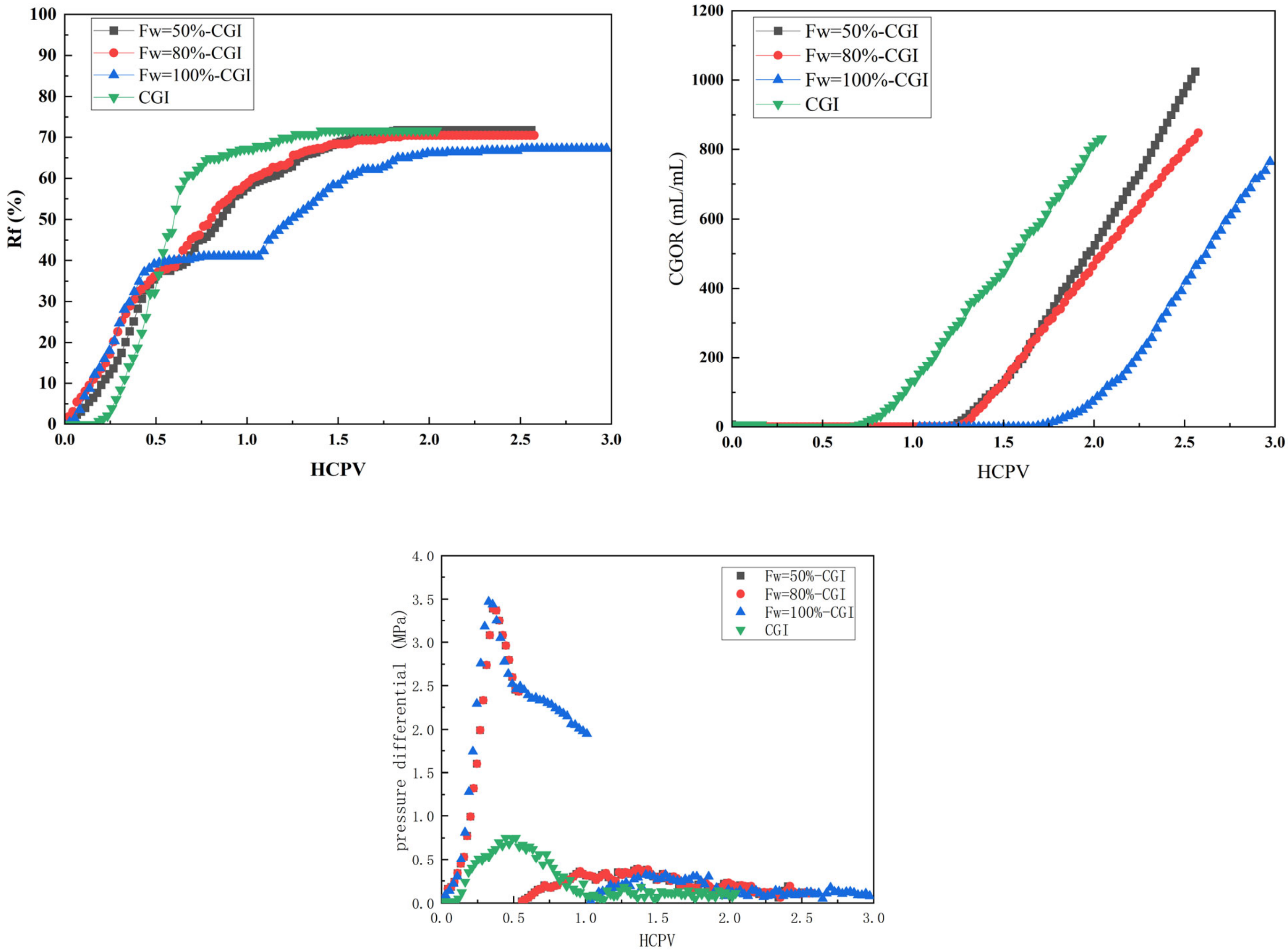

Figure 10. Core displacement experimental results of Class III reservoir cores.

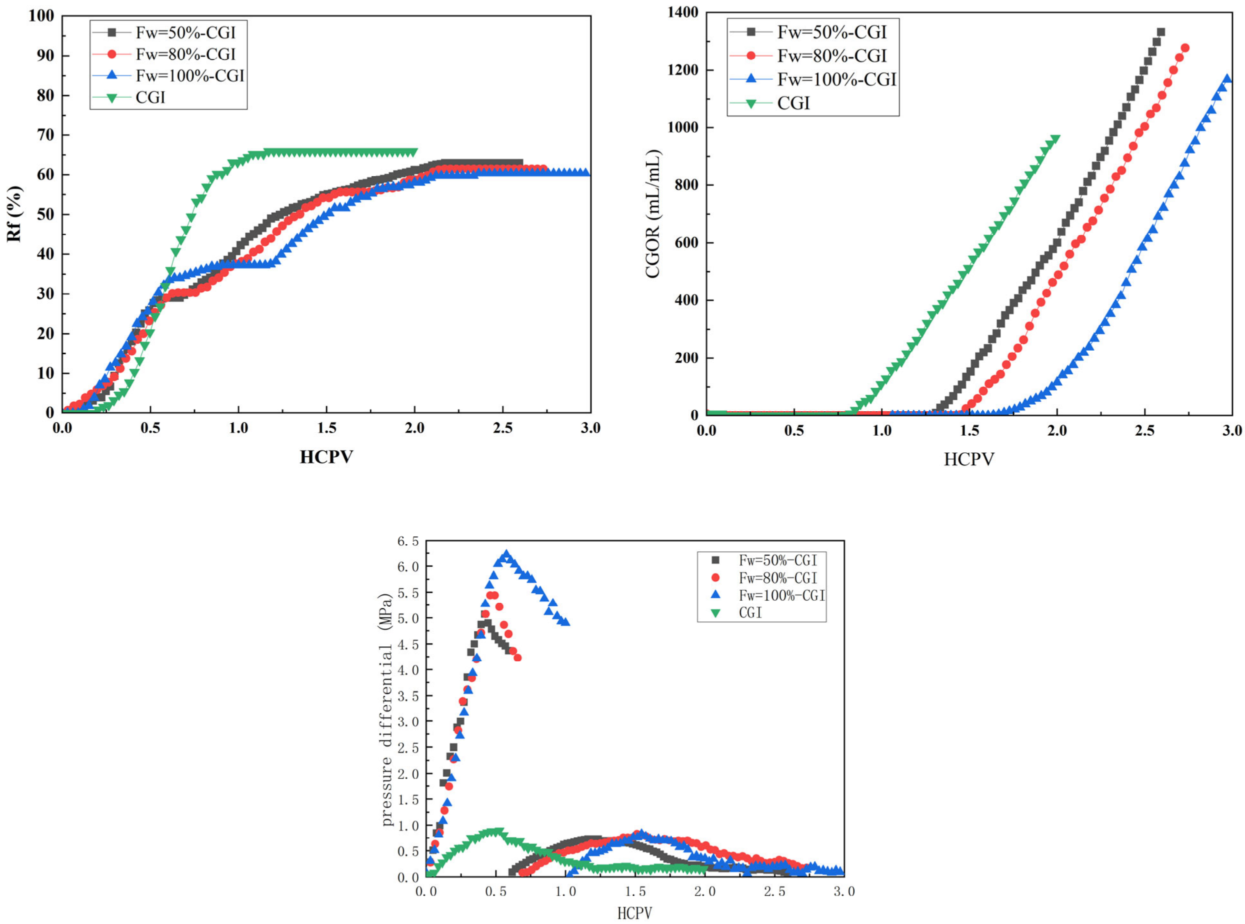

Figure 11. Core displacement experimental results of Class IV reservoir cores.

To better evaluate the incremental contribution of CO_2 under different switching schemes, Table 3 summarizes the waterflood recovery, incremental recovery by CO_2, final recovery, cumulative water injected, and oil produced per unit volume of injected CO_2 for each test. For Class II and III medium-to-high-permeability reservoirs, the F_w = 50% switching scheme yields the highest incremental recovery by CO_2 (40.54% and 34.18%, respectively) and the highest CO_2 utilization (0.160 and 0.116 mL/mL), significantly outperforming delayed switching schemes (0.108–0.133 mL/mL for Class II; 0.089–0.108 mL/mL for Class III). Notably, the cumulative water injected at F_w = 50% is only 0.44–0.53 PV, whereas at F_w = 100%, the cumulative water injected reaches 0.982–1.000 PV, yet the CO_2 incremental recovery drops to 27.36% and 26.24%, with CO_2 utilization as low as 0.108 and 0.089 mL/mL. This indicates that when switching is delayed to a high water cut, waterflooding has already established preferential flow paths, significantly reducing CO_2 efficiency. The CGI scheme achieves the highest final recoveries (75.53% and 71.60%) but lacks the mobility control provided by the water phase, leading to higher gas-channeling risks and potentially higher recycling costs in field practice. For Class IV low-permeability reservoirs, the post-waterflood switching schemes yield final recoveries of only 60.28–62.93%, with CO_2 utilization as low as 0.052–0.076 mL/mL. In contrast, the CGI scheme achieves a final recovery of 65.91% and a substantially higher CO_2 utilization (0.147 mL/mL), significantly outperforming all post-waterflood switching schemes. This is consistent with constraints imposed by water-locking effects and high capillary pressure on the CO_2 displacement efficiency in low-permeability reservoirs, further supporting the recommendation that low-permeability reservoirs should adopt early or direct CO_2 injection.

Table 3. Summary of recoveries and injection efficiencies for different switching schemes.

Reservoir Class	Switching Scheme	Waterflooding Recovery (%)	Incremental Recovery by CO_2 (%)	Final Recovery (%)	Cumulative Water Injected (PV)	Oil Produced per Volume of Injected CO_2 (mL/mL)
Class II (170 mD)	F_w = 50%	37.57	40.54	78.11	0.444	0.160
	F_w = 80%	39.48	33.65	73.13	0.516	0.133
	F_w = 100%	43.84	27.36	71.19	0.990	0.108
	CGI	/	75.53	75.53	/	0.298
Class III (80 mD)	F_w = 50%	37.52	34.18	71.70	0.534	0.116
	F_w = 80%	38.56	31.87	70.43	0.582	0.108
	F_w = 100%	40.99	26.24	67.23	0.982	0.089
	CGI	/	71.60	71.60	/	0.243
Class IV (10 mD)	F_w = 50%	29.02	33.91	62.93	0.593	0.076
	F_w = 80%	30.31	31.12	61.43	0.658	0.070
	F_w = 100%	37.22	23.06	60.28	1.000	0.052
	CGI	/	65.91	65.91	/	0.147

Regarding microscopic pore-throat mobilization, our results are in good agreement with Zhao et al. [36], who reported a recovery increment of 17.09–31.49% in micropore throats of medium-to-low-permeability cores after CO_2 miscible flooding, and with Su et al. [37], who demonstrated the mobilization capacity of CO_2 in nanopores (<3.7 nm). Specifically, for Class IV low-permeability cores, the recovery efficiency of micropores (<0.1 μm) increased from 5.8% after waterflooding to approximately 34.5% after CO_2 flooding, with an increment of 28.70%. In contrast to previous studies that often treated pore systems homogenously across different core types, our classified comparison reveals a distinct petrophysical hierarchy in T_2-inferred pore size mobilization: for Class II medium-to-high-permeability reservoirs, the incremental recovery is dominated by mesopores (0.1–1 μm, 31%), whereas for Class IV low-permeability reservoirs, the CO_2 contribution is heavily concentrated in micropores (<0.1 μm, 28.70%) and macropores (1–10 μm, 41%) that were previously bypassed during waterflooding. This suggests that CO_2 may target trapped remaining oil across different pore scales depending on reservoir petrophysical properties.

Regarding the transition timing, Liu et al. [20] recommended switching at a high-water-cut stage ($F_w \approx 82\%$) based on net present value (NPV) optimization, while Li and Gu [15] advocated an intermediate timing (when waterflooding recovery reaches 50% of its ultimate secondary recovery). Our classified experimental results further refine these earlier understandings: for Class II and III medium-to-high-permeability reservoirs, transitioning at F_w = 50% yields the highest ultimate recovery (78.11%), exceeding continuous gas injection (75.53%) and delayed switching at F_w = 100% (71.19%). For Class III medium-permeability reservoirs, the recovery at F_w = 50% (71.70%) is the highest among the tested post-waterflood switching schemes and is essentially comparable to continuous gas injection (71.60%, a negligible difference of only 0.10 percentage points, which does not constitute an outperformance) but is higher than delayed switching at F_w = 100% (67.23%). This favorable recovery performance among the tested schemes is mainly attributed to the mobility control provided by moderate movable water saturation before continuous water pathways are fully established (which represents an interpretation of production data rather than a measured saturation or relative-permeability effect). In contrast, for Class

IV low-permeability reservoirs, late switching is considered highly unfavorable, which may be partly related to high capillary resistance and water-locking effects, along with other possible factors, such as limited injectivity and poor phase connectivity. Direct CO_2 injection or very early transition achieves a significantly higher recovery (65.91%) than switching after complete waterflooding (61.43%). These findings demonstrate that the transition timing should not follow a single fixed threshold but requires differentiated optimization based on the interplay among the mobility ratio, gas channeling, and capillary resistance across different reservoir classes.

4. Discussion

This study has several limitations. First, the long-core switching experiments were not independently replicated due to limited core availability and because cleaning altered the pore structure and fluid distribution; similarly, the NMR pore-throat recoveries are single-core observations. Consequently, the recovery differences between the schemes and dynamic features observed on the differential pressure–HCPV curves are single-run laboratory observations and must not be treated as statistically established optima or differences. Second, the short-core NMR and long-core displacement experiments involve different length scales. Third, the T_2-to-pore-radius conversion is calibration-dependent and should be regarded as semi-quantitative; it delineates T_2-derived pore size classes rather than resolves discrete individual pores or directly proves nano-scale displacement. Fourth, $MnCl_2$ solution was used instead of representative formation water. Fifth, NMR cannot resolve phase topology or water film thickness. Sixth, a dedicated calibration of crude oil before and after CO_2 saturation was not performed; therefore, the possibility that CO_2 dissolution affects T_2 relaxation or signal distribution cannot be fully excluded, and the NMR results are interpreted as relative indicators rather than as absolute measures of oil production. Seventh, because the produced oil volume from the short cores was too small for precise outlet volumetric measurement, only a qualitative comparison between the produced oil volume and NMR-derived oil saturation changes was performed, and no rigorous quantitative mass balance validation was conducted; future work will improve micro-volume fluid collection methods. Eighth, only three discrete switching water-cut points were tested. Ninth, although the outlet backpressure (50 MPa) was set above the bulk slim-tube MMP (44 MPa), potential pore confinement effects and phase behavior shifts in tight micro-throats (especially in Class IV cores) may alter in situ miscibility such that tests should be interpreted under intended miscible conditions rather than definitively verified full miscibility throughout all pore spaces. Finally, reservoir-scale simulation and economic evaluation are required before field application. To further clarify the displacement mechanisms across different reservoir types, subsequent studies should introduce additional pore structure parameters, including tortuosity, cementation exponent, constriction factor, and pore connectivity. These parameters can improve the prediction accuracy of flow resistance and capillary barriers, especially for low-permeability reservoirs, and can further refine the class-specific injection strategies proposed in this work. Meanwhile, as the existing NMR, recovery, CGOR, and pressure datasets do not provide direct measurements of the 3-D pore connectivity, water film thickness, phase topology, relative permeability, channeling geometry, or capillary pressure, the CGOR and recovery curve shapes must be treated as indirect macroscopic indicators; descriptions of preferential flow or delayed breakthrough represent inferences consistent with production responses rather than directly measured in situ flow pathways. All mechanistic interpretations presented in this work are treated as data-consistent inferences rather than direct determinations of these properties and will be further refined in subsequent studies.

5. Conclusions

In this study, high-temperature and high-pressure core displacement experiments coupled with online NMR measurements were conducted to elucidate how the benefit of post-waterflooding CO_2 injection depends on the reservoir class and how NMR-scale pore-throat mobilization relates to macroscopic recovery. The primary conclusions are summarized as follows:

(1) NMR under intended miscible conditions confirms that CO_2 mobilizes oil within small T_2-derived pore size classes (<0.1 μm) across all reservoir types, showing the largest relative increase in Class IV micropores (from 5.8% to 34.5%). However, in long-core floods, high capillary resistance, water locking, and longer transport distances restrict the coalescence and flow of mobilized oil, resulting in negligible macroscopic incremental recovery for late switching in Class IV cores. Microscopic desaturation does not inherently guarantee proportional macroscopic recovery.

(2) The interaction between prior waterflooding and subsequent CO_2 injection is dictated by the reservoir properties. In Class II and III medium-to-high-permeability reservoirs, production responses at intermediate switching (F_w = 50%) are consistent with water–gas synergy, where the water phase is interpreted to provide mobility control that delays gas breakthrough. In Class IV low-permeability reservoirs, pre-existing water establishes barriers and capillary trapping that impair gas–oil contact, rendering late post-waterflood switching distinctly unfavorable compared to direct gas injection. (These mechanisms represent interpretations of production dynamics rather than measured in situ saturation or relative-permeability data.)

(3) Transition timing requires class-differentiated design rather than a single water-cut threshold. The following results were obtained under the tested conditions (Table 4): Class II (170 mD): Switching at F_w = 50% yielded the highest recovery among the tested conditions (78.11%), exceeding continuous gas injection (75.53%). Class III (80 mD): Switching at F_w = 50% achieved the highest recovery among the tested switching schemes (71.70%), comparable to continuous gas injection (71.60%, 0.10 percentage point difference), whereas delayed switching (F_w = 80% and 100%) reduced recovery. Class IV (10 mD): Post-waterflood switching yielded limited final recoveries (60.28–62.93%), with direct continuous gas injection achieving the highest recovery (65.91%). These single-run laboratory observations provide physical insights rather than field prescriptions; site-specific timing decisions require numerical simulation and economic evaluations.

Table 4. Comparison of best-performing scheme among those tested and key characteristics across reservoir classes.

Reservoir Class	Best-Performing Scheme Among Those Tested	Key Characteristics	Applicability
Class II (170 mD)	F_w = 50%	Large pore throats; rapid waterflood sweep; ideal water–gas synergy	Recovery exceeded CGI under tested conditions; may be favorable for reservoirs with similar petrophysical properties
Class III (80 mD)	F_w = 50%	Moderate pore throats; balanced oil–water mobility	Yielded highest recovery among tested switching schemes and comparable to CGI (71.70% vs. 71.60%); delayed switching resulted in lower recovery
Class IV (10 mD)	Early or direct CGI	Fine pore throats; high capillary resistance; severe water locking	Post-waterflood switching yielded limited incremental recovery in this study; direct CO_2 injection may be considered

https://doi.org/10.3390/en19184432

Supplementary Materials: The following supporting information can be downloaded at: https://www.mdpi.com/article/10.3390/en19184432/s1, Figure S1: Differential pressure curves; Table S1: Sensitivity analysis of pore-throat classification thresholds.

Author Contributions: Data curation, Y.X.; formal analysis, Z.L.; methodology, H.W. (Hongmei Wang), Y.L.; conceptualization, Y.L.; resources, Y.L.; validation, H.W. (Hongtao Wang); writing—original draft, Y.S.; writing—review and editing, H.C. All authors have read and agreed to the published version of the manuscript.

Funding: This research received no external funding.

Data Availability Statement: The data presented in this study are available upon request from the corresponding author. (The data are not publicly available due to confidentiality agreements of the oilfield company project).

Conflicts of Interest: Authors Hongmei Wang, Hong Chen, Hongtao Wang, Yafan Xing and Zhaoyang Lu were employed by the Huabei Oilfield Company. The remaining authors declare that the research was conducted in the absence of any commercial or financial relationships that could be construed as potential conflicts of interest.

References

1. Yu, H.; Wang, Y.; Huang, K.; Zhu, Y.; Wang, B.; Wen, X.; Wang, P.; Lyu, Z.; Dai, Q. Evaluation Methods and Development Direction of Microscopic Residual Oil by Water Flooding in Low Permeability Sandstone Reservoirs. *Pet. Geol. Recovery Effic.* **2024**, *36*, 17–27. (In Chinese)
2. Wang, G.; Xiao, W.; Wang, J.; Song, P.; Zheng, L.; Zhang, X.; Zheng, D. Microscopic Waterflooding and Residual Oil Distribution Characteristics in Ultra-Low Permeability Sandstone. *Rock Miner. Anal.* **2026**, *45*, 142–159. (In Chinese)
3. Liu, X.; Chen, K.; Ma, L.; Li, J.; He, W.; Yang, F.; Li, Y.; Hong, X.; Zheng, Z. Research on Distribution Characteristics and influencing Factors of Remaining Oil in Water Flooding Based on Micro CT Scanning. *Contemp. Chem. Ind.* **2024**, *53*, 2302–2308. (In Chinese)
4. Ren, M.; Shi, Q.; Xin, H.; Liu, Z.; Zhou, Z. Characteristics of Remaining Oil Distribution in Conglomerate Reservoirs after Water Flooding and Technical Countermeasures. *Spec. Oil Gas. Reserv.* **2023**, *30*, 147–153. (In Chinese)
5. Tao, L.; Sun, M.; Xu, Z.; Yang, K.; Zhu, Q.; Shi, W.; Bai, J.; Xu, Y.; Zha, W. Current status and future prospects of CO_2-enhanced recovery technologies for unconventional oil and gas reservoirs based on carbon peaking and carbon neutrality goals. *Youqi Dizhi Yu Caishoulu* **2026**, *33*, 144–157. [CrossRef]
6. Yu, W.; Lashgari, H.R.; Wu, K.; Sepehrnoori, K. CO_2 injection for enhanced oil recovery in Bakken tight oil reservoirs. *Fuel* **2015**, *159*, 354–363. [CrossRef]
7. Feng, H.; Haidong, H.; Yanqing, W.; Jianfeng, R.; Liang, Z.; Bo, R.; Butt, H.; Shaoran, R.; Guoli, C. Assessment of miscibility effect for CO_2 flooding EOR in a low permeability reservoir. *J. Pet. Sci. Eng.* **2016**, *145*, 328–335. [CrossRef]
8. Su, Y.; Wu, X.; Hou, Y.; Hou, Z. Mechanism of CO_2 miscible displacement in low permeability reservoir and influencing factor. *J. China Univ. Pet. (Ed. Nat. Sci.)* **2011**, *35*, 99–102. (In Chinese)
9. Wei, B.; Gao, H.; Pu, W.; Zhao, F.; Li, Y.; Jin, F.; Sun, L.; Li, K. Interactions and phase behaviors between oleic phase and CO_2 from swelling to miscibility in CO2-based enhanced oil recovery (EOR) process: A comprehensive visualization study. *J. Mol. Liq.* **2017**, *232*, 277–284. [CrossRef]
10. Li, Z.; Gu, Y. Soaking effect on miscible CO_2 flooding in a tight sandstone formation. *Fuel* **2014**, *134*, 659–668. [CrossRef]
11. Kumar, N.; Augusto Sampaio, M.; Ojha, K.; Hoteit, H.; Mandal, A. Fundamental aspects, mechanisms and emerging possibilities of CO_2 miscible flooding in enhanced oil recovery: A review. *Fuel* **2022**, *330*, 125633. [CrossRef]
12. Guo, L. Laboratory investigation on CO_2 miscible displacement on special low-permeability reservoirs, Yi34 block, Bonan oilfield. *Pet. Geol. Recovery Effic.* **2011**, *18*, 37–40+113. (In Chinese)
13. Xiao, P.; Yang, Z.; Wang, X.; Dai, X. A laboratory study on the micro mechanism of oil displacement with CO_2 flooding. *Xinan Shiyou Daxue Xuebao/J. Southwest Pet. Univ.* **2015**, *37*, 161–165. [CrossRef]
14. Zhou, L.; Liu, Y.; Zhao, C.; Wang, W.; Yan, Y. Molecular Insights into the EOR Mechanism of Water, CO_2, and CO_2–WAG Flooding in Heterogeneous Nanochannels: A Molecular Dynamic Simulation. *Langmuir* **2025**, *41*, 6050–6064. [CrossRef]
15. Li, Z.; Gu, Y. Optimum Timing for Miscible CO_2-EOR after Waterflooding in a Tight Sandstone Formation. *Energy Fuels* **2014**, *28*, 488–499. [CrossRef]
16. Aminu, M.D.; Nabavi, S.A.; Rochelle, C.A.; Manovic, V. A review of developments in carbon dioxide storage. *Appl. Energy* **2017**, *208*, 1389–1419. [CrossRef]

17. He, Y.; Yang, M.; Qin, J.; Tang, Y.; Qiu, S. Advances of CO_2 channeling control technologies for enhanced oil recovery and storage efficiency. *Fuel* **2027**, *428*, 140193. [CrossRef]
18. Li, L.; Kang, Y.; Liu, F.; Hu, Y.; Huang, Y.; Wu, S. Experimental study on the mass transfer and microscopic distribution characteristics of remaining oil and CO_2 during water-miscible CO_2 flooding. *J. CO_2 Util.* **2024**, *87*, 102920. [CrossRef]
19. Xia, Z.; Yin, H.; Wang, X.; Li, Z. Simulation Study on the Displacement Characteristics of an Ultra-Low Permeability Reservoir by CO_2-WAG Flooding. In *Mechanisms and Machine Science*; Springer International Publishing: New York, NY, USA, 2023; pp. 697–713. [CrossRef]
20. Liu, J.; Meng, F.; Zhao, H.; Xu, Y.; Wang, K.; Shi, C.; Chen, Z. Optimization of CO_2 EOR and geological sequestration in high-water cut oil reservoirs. *J. Pet. Explor. Prod. Technol.* **2024**, *14*, 1491–1504. [CrossRef]
21. Bikkina, P.; Wan, J.; Kim, Y.; Kneafsey, T.J.; Tokunaga, T.K. Influence of wettability and permeability heterogeneity on miscible CO_2 flooding efficiency. *Fuel* **2016**, *166*, 219–226. [CrossRef]
22. Dai, C.; Zou, C.; Liu, Y.; Yang, N.; Wu, Y.; Zhao, G.; Yuan, B.; Huang, Y. Progress and future directions in channeling control technologies for CO_2 flooding. *Zhongguo Shiyou Daxue Xuebao (Ziran Kexue Ban)/J. China Univ. Pet. (Ed. Nat. Sci.)* **2025**, *49*, 85–96. [CrossRef]
23. He, J.; Ke, W.; Zhu, X.; Zhen, M.; Liu, T. Research on Enhanced Oil Recovery by CO_2 Water/Polymer Composite Alternative Flooding in Heterogeneous Reservoirs. *ACS Omega* **2025**, *10*, 51272. [CrossRef]
24. Yan, Y.; Lyu, W.; Yu, H.; Lv, W.; Ni, S. Mechanisms of CO_2 flooding front migration and injection-production regulation in heterogeneous reservoirs: A large-scale visual physical simulation study. *J. CO_2 Util.* **2026**, *105*, 103339. [CrossRef]
25. Wang, R.; Zhang, Y.; Lyu, C.; Lun, Z.; Cui, M.; Lang, D. Displacement characteristics of CO_2 flooding in extra-high water-cut reservoirs. *Energy Geosci.* **2024**, *5*, 100115. [CrossRef]
26. Qian, C.; Rui, Z.; Liu, Y.; Zhou, K.; Du, K.; Zhao, Y.; Zou, J.; Song, K.; Li, X. Microfluidic investigation on microscopic flow and displacement behavior of CO_2 multiphase system for CCUS-EOR in heterogeneous porous media. *Chem. Eng. J.* **2025**, *505*, 159135. [CrossRef]
27. Hu, W.; Lü, C.; Wang, R.; Cui, M.; Yang, Y.; Wang, X. Porous flow mechanisms and mass transfer characteristics of CO_2 miscible flooding after water flooding. *Shiyou Xuebao/Acta Pet. Sin.* **2018**, *39*, 201–207. [CrossRef]
28. Cui, M.; Wang, R.; Lü, C.; Lun, Z.; Zhao, S.; Wang, Y.; Tang, Y. Research on microcosmic oil displacement mechanism of CO_2 flooding in extra-high water cut reservoirs. *Zhongguo Shiyou Daxue Xuebao (Ziran Kexue Ban)/J. China Univ. Pet. (Ed. Nat. Sci.)* **2018**, *42*, 119–125. [CrossRef]
29. Lu, P.; Yan, Z.; Lai, J.; Wang, K. Molecular insight into oil displacement by CO_2 flooding in water-cut dead-end nanopores. *RSC Adv.* **2024**, *14*, 25385–25392. [CrossRef]
30. Wang, Y.; Bao, Z.; Li, Z.; He, S.; Fang, F. High-temperature and high-pressure online nuclear magnetic resonance testing for CO_2 flooding in Daqingzijing Oilfield. *Front. Earth Sci.* **2025**, *13*, 1556179. [CrossRef]
31. Jin, X.; Du, M.; Hao, C.; Xin, F.; Kang, P.; Lü, W.; Yao, L. Characteristics and CO_2 flooding enhanced oil recovery experiments of Chang 6 in Ordos Basin. *Youqi Dizhi Yu Caishoulu* **2025**, *32*, 125–137. (In Chinese)
32. Wang, X.; Yang, Z.; Li, H.; Li, Z. Microscopic distribution of remaining oil of ultra-low permeability reservoir by using NMR technique. *Yingyong Jichu Yu Gongcheng Kexue Xuebao/J. Basic Sci. Eng.* **2013**, *21*, 702–709. [CrossRef]
33. Siavashi, J.; Najafi, A.; Sharifi, M.; Fahimpour, J.; Shabani, M.; Liu, B.; Liu, K.; Yan, J.; Ostadhassan, M. An insight into core flooding experiment via NMR imaging and numerical simulation. *Fuel* **2022**, *318*, 123589. [CrossRef]
34. Xiao, P.; Yang, Z.; Wang, X.; Xiao, H.; Wang, X. Experimental investigation on CO_2 injection in the Daqing extra/ultra-low permeability reservoir. *J. Pet. Sci. Eng.* **2017**, *149*, 765–771. [CrossRef]
35. Zhao, Y.; Zhang, Y.; Lei, X.; Zhang, Y.; Song, Y. CO_2 flooding enhanced oil recovery evaluated using magnetic resonance imaging technique. *Energy* **2020**, *203*, 117878. [CrossRef]
36. Zhao, Y.; Yu, Z.; Dang, X.; Shen, G.; Lu, J. In-situ dynamic characterization of residual oil displacement mechanism by CO_2 after water flooding using online nuclear magnetic resonance. *Oil Drill. Prod. Technol.* **2025**, *47*, 569–578. (In Chinese) [CrossRef]
37. Su, Y.; Zhao, C.; Li, X.; Wang, X.; Zhang, J.; Huang, B.; Tian, X.; Liu, M.; Song, K. A New Transformation Method of the T2 Spectrum Based on Ordered Clustering—A Case Study on the Pore-Throat Utilization Rule of Supercritical CO_2 Flooding in Low Permeability Cores. *Appl. Sci.* **2025**, *15*, 730. [CrossRef]
38. Qi, D.; Ma, T.; Li, C.; Guo, C.; Yuan, Y.; Wang, Z. A comprehensive analysis of factors influencing CO_2-oil displacement in sandstones under reservoir conditions by online nuclear magnetic resonance testing. *Sci. Rep.* **2026**, *16*, 23695. [CrossRef]

https://doi.org/10.3390/en19184432